JOURNAL OF GEOPHYSICAL RESEARCH: OCEANS, VOL. 118, 1333–1348, doi:10.1002/jgrc.20067, 2013

Direct observations of the Antarctic circumpolar current transport on the northern flank of the Kerguelen Plateau

G. M. Damerell,[1] K. J. Heywood,[1] and D. P. Stevens[2]

Received 15 August 2012; revised 19 December 2012; accepted 20 December 2012; published 20 March 2013.

[1] The standing meander in the Antarctic Circumpolar Current (ACC) found on the northern flank of the Kerguelen Plateau was investigated during the Southern Ocean Finestructure cruise in November–December 2008. An 18 year time series of surface geostrophic currents from satellite altimetry shows that the meander as observed during this survey is typical of the region. Hydrographic stations were occupied between 65–75°E and 43–48°S on the shelf (~200 m depth) and slope into the deep ocean to the north of Kerguelen (~4700 m), providing the most detailed survey of this region to date. Geostrophic shears are referenced to lowered acoustic Doppler current profiler velocities to give the first estimate of the total volume transport in this region, and the transport budget is closed around the survey box. The Subtropical Front, Subantarctic Front, and a northern branch of the Polar Front together have an associated transport of 174 ± 22 Sv eastward. While 174 Sv is large compared with typical Drake Passage transports, it is reconciled with other estimates of the total transport with the additional 15 Sv of the Indonesian Throughflow. Baroclinic transport referenced to the deepest common level between station pairs is 119 Sv, consistent with other estimates of the baroclinic transport in this area. At this longitude, the fronts of the ACC are exceptionally close together. We discuss the exchange of properties across the fronts.

Citation: Damerell, G. M., K. J. Heywood, and D. P. Stevens (2013), Direct observations of the Antarctic circumpolar current transport on the northern flank of the Kerguelen Plateau, *J. Geophys. Res. Oceans*, *118*, 1333–1348, doi:10.1002/jgrc.20067.

1. Introduction

[2] The Kerguelen Plateau is a volcanic ridge which forms the largest submarine plateau in the Southern Ocean (Figure 1). It spans approximately 16° in latitude, from ~65°E, 46°S, southeast (S.E.) to ~85°E, 62°S, and is divided, at around 55–57°S, into the Northern and Southern Kerguelen Plateaus (NKP and SKP) by the Fawn Trough (FT), which has a sill depth of ~2600 m. The NKP includes the Kerguelen Islands towards the north end and the Heard/McDonald Islands towards the south. Further south, at 85°E, 63–66°S, the Princess Elizabeth Trough (PET, sill depth ~3750 m), lies between the SKP and Antarctica.

[3] The circulation around the plateaus and the flows through locally deeper troughs in the plateaus has long been a topic of study, yet many aspects remain to be quantified. Figure 1 provides a synthesis of the historical studies listed in Table 1. Figure 1 and Table 1 together summarize the main currents in the Indian Ocean sector of the Southern Ocean, as well as the flows around the Crozet and Kerguelen Plateaus. This is not a definitive collection of all studies in this region, simply a summary based, where possible, on more recent studies in which the use of acoustic Doppler current profilers (ADCPs) to reference geostrophic shear allows estimates of total geostrophic transport. The hydrographic survey of *Park et al.* [1993] in the Crozet Basin (which included the region north of the Kerguelen Plateau discussed in the current study) did not use ADCPs and so found transport relative to the deepest common layer, which we will henceforth refer to as baroclinic transport.

[4] The Kerguelen Plateau constitutes a significant topographic barrier for the Antarctic Circumpolar Current (ACC). The ACC is associated with several main eastward flowing frontal jets, generally designated as the Subantarctic Front (SAF), Polar Front (PF), Southern ACC Front (SACCF), and Southern Boundary (SB) of the ACC [*Orsi et al.*, 1995]. Table 2 lists hydrographic characteristics by which these fronts are typically identified. Throughout this paper, we use conservative temperature and absolute salinity rather than in-situ temperature and practical salinity [*IOC et al.*, 2010], though both practical and absolute salinity are given in Table 2 to facilitate comparison with other works. Conservative temperature in this region differs from potential temperature by a maximum of 0.02 °C and an average of 2×10^{-5} °C, so they can be treated as virtually identical. We also use water mass definitions based on neutral density (γ^n, in kg m^{-3}, as defined by *Jackett and McDougall* [1997]), with consideration also given to definitions based on hydrographic properties (Table 3). The units of density (kg m^{-3}) are omitted henceforth.

[1]School of Environmental Sciences, University of East Anglia, Norwich UK.
[2]School of Mathematics, University of East Anglia, Norwich UK.

Corresponding author: G. M. Damerell, School of Environmental Sciences, University of East Anglia, Norwich, NR4 7TJ, UK. (g.damerell@uea.ac.uk)

2169-9275/13/10.1002/jgrc.20067

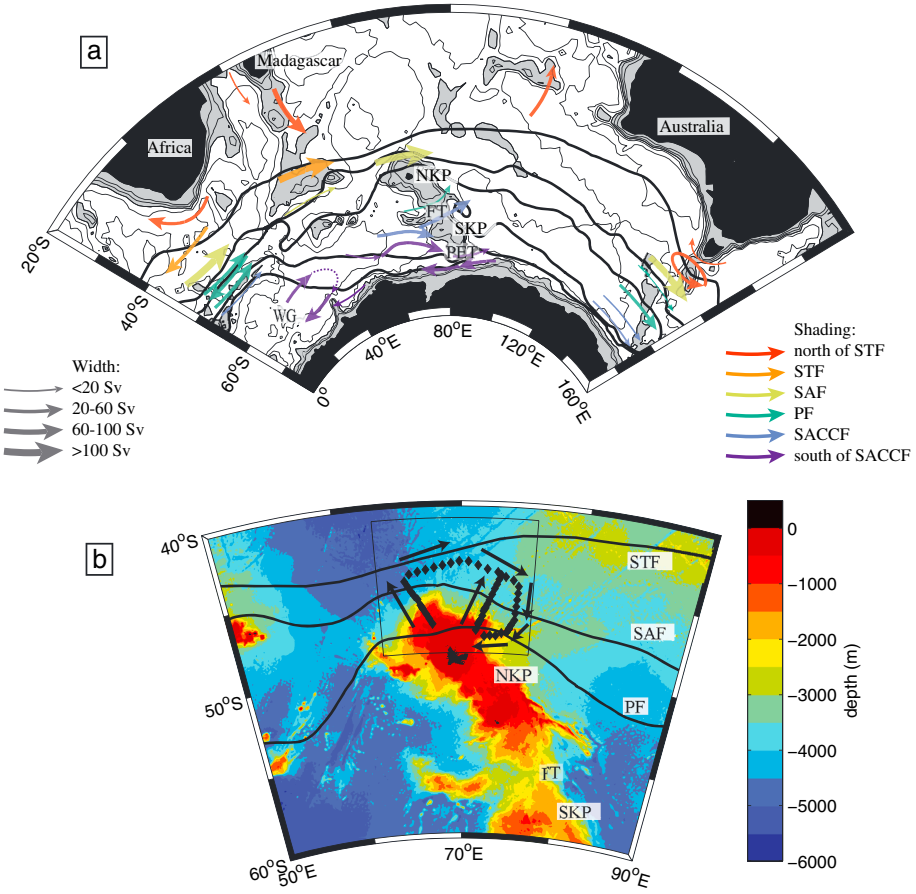

Figure 1. (a) Regional map, with smoothed bathymetry from *Smith and Sandwell* [1997]. Contours are every 1000 m, with gray shading to 3000 m deep. Various topographical features are indicated: NKP = North Kerguelen Plateau, SKP = South Kerguelen Plateau, FT = Fawn Trough, PET = Princess Elizabeth Trough. WG refers to the Weddell Gyre. Arrows represent currents from a variety of studies, listed in Tables 1 and 2. The width of the arrows represents the top-to-bottom transport and the shading the north-south position relative to the main ACC fronts. Where the arrows representing the Weddell Gyre are dotted, the flow pattern is inferred due to the lack of observational data. The thick black lines are the climatological mean positions of the fronts from *Orsi et al.* [1995]: from north to south, the STF, SAF, PF, SACCF, and SB. (b) Bathymetry of the NKP, showing the location of the stations occupied in the SOFine survey (black diamonds). The seven black arrows indicate the direction of the ship track along the seven transects, which is the order in which stations are shown in subsequent figures plotted against depth. The thin black lines outline the area shown in subsequent plan view figures. Topographic features and climatological mean positions of the fronts are indicated as in Figure 1a.

[5] The extent of the ACC is usually defined in terms of the circumpolar waters that pass through Drake Passage. Further south are various gyres (e.g., Weddell Gyre, Ross Sea Gyre), and the Antarctic Slope Front/Current (ASF), found above the continental slope around most of Antarctica associated with a westward flowing frontal jet. North of the SAF is the eastward flowing jet associated with the Subtropical Front (STF), which separates Subtropical Surface Water (STSW) from Subantarctic Surface Water (SASW). Within the Indian Ocean sector of the Southern Ocean, the Agulhas Return Front (ARF) is found to the north of the STF. The ARF encloses the warm and saline thermocline waters of the subtropical gyre in the South Indian Ocean.

[6] In the South Indian Ocean, *Park et al.* [1993] used Conductivity–Temperature–Depth (CTD) data, taken on a cruise in April–May 1991, to find the STF and SAF blended together on the northern flank of the Kerguelen Plateau, giving a concentrated jet centered at 44–45°S with a baroclinic transport of ~100 Sv. (Their criteria for the SAF are, however, different to those in Table 2, being θ/S ranges of 4–8 °C and 34.1–34.5 at 200 m. They do, however, comment that at the southward edge of this jet, there is a rapid descent of the subsurface salinity minimum, corresponding to the SAF definition of *Orsi et al.* [1995].) *Sparrow et al.* [1996], using the hydrographic atlas published by *Olbers et al.* [1992] and the same front definitions as *Orsi et al.* [1995], similarly find a blended STF/SAF on the northern flank of the Kerguelen Plateau with a baroclinic transport of ~110 Sv.

[7] The location of the PF (or Fronts) is considerably more in question. It is now fairly common to consider a surface and subsurface expression of the PF in hydrographic surveys, as was done by *Sparrow et al.* [1996]. Several studies have argued that each of the three primary ACC fronts

Table 1. Front Locations and Transports in the Indian Ocean From Various Hydrographic Surveys, as Shown on Figure 1[a]

Location	Data	Fronts/Transport	Reference
SR2, from S. Africa to Antarctica, ~10°E	HS in 2004. GVs referenced to LADCPs.	SACCF at 53°S, 12 Sv. Two branches of PF at ~50 and 52°S (33 and 30 Sv, respectively), with westward flow (−28 Sv) between. SAF at ~43 − 49°S, 107 Sv. Bottom intensified westward flow beneath STF, plus eddies (Agulhas leakage) give total transport of −42 Sv between 43°S and the coast of Africa.	*Gladyshev et al.* [2008]
Weddell Gyre at 30°E, south of 58°S	Two HSs in 1993 and 1996. GVs referenced to VMADCP at 50 m depth.	Weddell Gyre transporting ~40 Sv between 58 and 65°S, and ~−40 Sv (i.e., westward) between 65 and 69°S.	*Park et al.* [2001]
Region south of 60°S, and 30–80°E	HS in 2006. Transport calculated from LADCP velocities.	ASF at 30°E, 67–69°S, −18 Sv. ASF at 80°E, 65–66°S, −28 Sv. SB at 50°E, 62–65°S, 15 Sv. SB and SACCF at 80°E, 62–65°S, >40 Sv. Difficulty estimating the transport of the Weddell Gyre as it appeared to break mass conservation.	*Meijers et al.* [2010]
25°S, Africa to Madagascar	Hydrographic inverse box model.	14 ± 6 Sv southward.	*Ganachaud et al.* [2000]
Crozet Basin, 40–80°E, 37–52°S	HS in 1991. GVs referenced to deepest common layer.	SAF/PF, 47–50°S 50–55°E (north of Crozet), 15 Sv. Shaded in Figure 1 as SAF. ARF/STF/SAF, 41–44°S 50–55°E, 130 Sv. Shaded in Figure 1 as STF. STF/SAF, 44–46°S 70°E, (north of NKP), 95 Sv. Shaded in Figure 1 as SAF. ARF-waters peel off to north from 50 to 80°E, 35 Sv.	*Park et al.* [1993]
Fawn Trough (FT), 72–86°E, 53–58°S	HS in 2009. Transport calculated from LADCP velocities.	SACCF, 55–57°S, 43 Sv. PF, 55°S, just south of Heard/McDonald Islands, 6 Sv.	*Park et al.* [2009]
Flow in PET, 85°E, 63–65°S	HS in 1993 and 1994. GVs referenced to VMADCP at 100–400 m depth.	ASF and associated westward flow, 65–66°S, −45 Sv. SACCF and SB, 63–65°S, 11 Sv.	*Heywood et al.* [1999]
32°S across entire Indian Ocean Basin	Hydrographic inverse box model, using GVs referenced to LADCP/VMADCP.	Complicated structure with many local north/southward flows. Summarized as 70 Sv southward in the western part of the basin, and 52 Sv northward in the eastern part. The arrows on Figure 1 are merely in the center of these broad regions and do not indicate locally intense flows.	*McDonagh et al.* [2008]
SR3, from Tasmania to Antarctica, ~140°E	Six HSs between 1991 and 1996. GVs referenced to "best guess" reference layer.	SACCF-south at 64°S, 11 ±3 Sv, SACCF-north at 62°S, 18 ±3 Sv. PF-south at 59°S, 24 ±3 Sv, PF-north at 53–54°S, 5 ±5 Sv. SAF at 51–52°S, 105 ±7 Sv. Subantarctic Zone Recirculation, ~44 − 49°S, 22 ±8 Sv (net transport zero). Tasman outflow immediately south of Tasmania, −8 ±13 Sv.	*Rintoul and Sokolov* [2001]

[a]Here listed from West to East, and from South to North. HS = hydrographic survey, GVs = geostrophic velocities.

actually consists of multiple branches or filaments (for example, *Holliday and Read* [1998], *Sokolov and Rintoul* [2007], and *Sokolov and Rintoul* [2009]). The flow through the FT has been ascribed to the surface expression of the PF (or south PF) [*Sparrow et al.*, 1996; *Moore et al.*, 1999; *Holliday and Read*, 1998; *van Wijk, et al.*, 2010], multiple branches of the PF and SACCF [*Sokolov and Rintoul*, 2009], or the SACCF alone [*Park et al.*, 2009]. The latter, to our knowledge, describe the only survey to date which crossed the FT and made use of direct current measurements from ADCPs, enabling them to find a total eastward transport of 43 Sv through the FT. *Sparrow et al.* [1996] and *Holliday and Read* [1998] place the subsurface expression of the PF to the north of the Kerguelen Islands, with warmer surface temperatures than the surface PF. Another group [*Park et al.*, 1993; *Charrassin et al.*, 2004; *Park et al.*, 2008a, 2008b, 2009; *Roquet et al.*, 2009] report finding the subsurface PF broken into multiple filaments passing through various locally deeper troughs in the NKP with a combined transport of 8 Sv, none of which passes to the north of the Kerguelen Islands. *van Wijk et al.* [2010] infer the presence of the subsurface PF (or north PF) to the north of the Kerguelen Islands, having found that front on the eastern side of the NKP with an associated baroclinic transport of 25 Sv to the S.E.

[8] *Moore et al.* [1999] and *Sokolov and Rintoul* [2009] suggest that the location of the PF has varied over time. Using satellite observations of sea surface temperature (SST), *Moore et al.* [1999] mapped the location and dynamics of the surface PF from 1987 to 1993. The mean path of the surface signature of the PF goes through the FT, in agreement with *Sparrow et al.* [1996] and *Holliday and Read* [1998], but there is a very wide latitudinal range (nearly 10°), including, at times, north of the Kerguelen Islands, in agreement with *Orsi et al.* [1995]. The analysis of *Sokolov and Rintoul* [2009] is based on sea surface height (SSH) gradient fields from satellite altimetry data taken between 1992 and 2007. The feature they identify as the northernmost branch of the PF shifted from passing to the

Table 2. Summary of Front Identification Criteria After *Orsi et al.* [1995] and *Sparrow et al.* [1996], and Used Throughout Unless Otherwise Stated in the Text. Conservative Temperature ($\boldsymbol{\Theta}$, in °C), Absolute Salinity ($\boldsymbol{S_A}$, in g kg^{-1}), Practical Salinity ($\boldsymbol{S_p}$, in psu), and Dissolved Oxygen (O_2, in μmol l^{-1})

Front	Criteria
Agulhas Return Front (ARF)	Θ range 12–16 °C at 200 m
Subtropical Front (STF)	$\Theta/S_A(S_p)$ ranges of 10–12 °C and 34.77–35.17(34.6–35.0) at 100 m
Subantarctic Front (SAF)	rapid descent of subsurface S-min to 500–600 m depth
Polar Front (PF)- subsurface	northern terminus of 2 °C isotherm below 200 m
Polar Front (PF)- surface	max gradient of SST regime between 2 and 6°
Southern ACC Front (SACCF)	Θ >1.8 °C along Θ-max at depths >500 m to the north $S_A(S_p)$ >34.9(34.73) along S-max at depths >800 m to the north Θ <0 °C along Θ-min at depths <150 m to the south
Southern Boundary (SB)	southern limit of UCDW—high nutrient and low $O_2 < 200$ μmol l^{-1} at 27.35 $<\sigma_0 <$27.75

north of the Kerguelen Plateau between 1992 and 2003, to passing through the FT from 2004 to 2007, a meridional shift of nearly 10°. They link this to the increase in average SSH in the Southern Ocean, indicating that the fronts are moving poleward.

[9] Prior to the Southern Ocean Finestructure project (SOFine) discussed here, there was a lack of high-resolution hydrographic data in the region north of the Kerguelen Plateau. The survey discussed by *Park et al.* [1993] had a limited number of stations (16 stations in the area in which the SOFine survey had 60 stations), and the work of *Orsi et al.* [1995] and *Sparrow et al.* [1996] was based on hydrographic atlas data so give climatological means rather than a realization over a short time period. No previous studies on the north flank of the Kerguelen Plateau, to our knowledge, have included ADCP measurements to provide a level of known motion, so assumptions of a level of no motion have been necessary. The location and transport of the PF—or at least a northern branch of the PF—is also uncertain. A further unknown is whether the merging/bunching of fronts in a narrow meridional extent leads to the exchange of properties across the fronts.

[10] The organization of this paper is as follows: section 2 describes the data and methods, section 3 discusses the various water masses observed, section 4 discusses the fronts and associated transports, section 5 discusses the total transport through the region and compares this with other observations in the ACC, section 6 discusses the horizontal and vertical exchange of properties, and section 7 contains the conclusions.

2. Data and Methods

[11] The SOFine project studied an area on the northern flank of the Kerguelen Plateau, where two main jets of the ACC form a large standing meander in climatological atlases and ocean circulation models [*Sparrow et al.*, 1996; *Sokolov and Rintoul*, 2009]. The SOFine survey [*Naveira Garabato*, 2009], undertaken onboard the RRS James Cook (Cruise number JC029) in November and December 2008, consisted

Table 3. Water Mass Definitions by Neutral Density (γ^n, in kg m^{-3}, as Defined by *Jackett and McDougall*, 1997) and Various Hydrographic Properties: Θ, $S_A(S_p)$ and O_2 as in Table 2

Water Mass	γ^n	References	Alternative Criteria	References
Antarctic Bottom Water (AABW)	>28.27	*Orsi et al.* [1999]	Θ<0 $S_A(S_p)$<34.9(34.73) O_2>223	*Heywood et al.* [1999]
ACC Bottom Water (AACbw)	28.18–28.27	*Orsi et al.* [1999]		
Lower Circumpolar Deep Water (LCDW)	27.98–28.18	adapted from σ_0 in *Heywood et al.* [1999]	$S_A(S_p)$>34.87(34.7), nutrient min	*Orsi et al.* [1995]
Upper Circumpolar Deep Water (UCDW)	27.55–27.98	adapted from σ_0 in *Sievers and Nowlin* [1984]	$O_2 < 200$ nutrient max	*Sievers and Nowlin* [1984]
Antarctic Intermediate Water (AAIW)	27.13–27.55	*Smith et al.* [2010] & *Heywood and King* [2002]	S min	*Deacon* [1937]
Subtropical Surface Water (STSW)	<27.13		Θ>12 $S_A(S_p)$>35.27(35.1) $O_2 < 270$	*Park et al.* [1993]
Subantarctic Surface Water (SASW)	<27.13		5<Θ<9 $S_A(S_p)$<34.16(34.0) $290 < O_2 < 315$	*Park et al.* [1993]
Antarctic Surface Water (AASW)	<27.13		Θ<5 $S_A(S_p)$<34.16(34.0) O_2>315	*Park et al.* [1993]

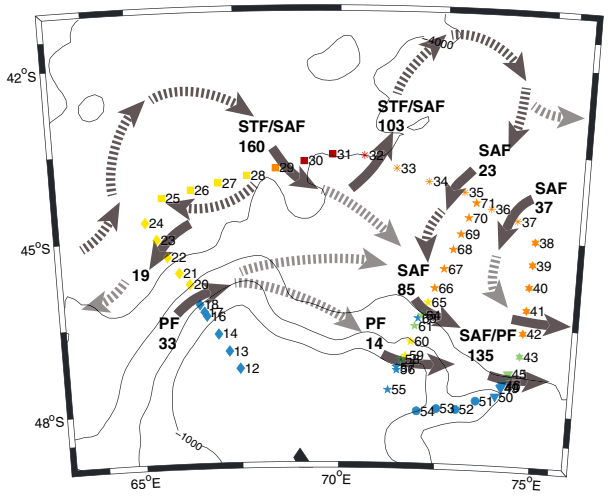

Figure 2. Station locations, with approximate jet locations and full-depth transports (Sv), as discussed in the text. Solid arrows indicate direct current measurements (LADCP). Black dashed arrows indicate areas where the surface current direction is taken from satellite altimetry, but we have no direct measurements of the full-depth transport from hydrographic sections. Gray dashed arrows indicate areas where the current direction is inferred; necessary because the currents as indicated by satellite altimetry are very weak, change during the course of the cruise, or are not consistent with mass conservation. Transects are shown as western (diamonds), northern transect I (squares), northern transect II (asterisks), eastern (six-pointed stars), southeastern (triangles), southern (circles), and central (five-pointed stars). The colors indicate the surface water (based on the average properties of the top 100 m): blue = AASW, green = intermediate properties between AASW and SASW, yellow = SASW, orange = intermediate properties between SASW and STSW, red = STSW (see Table 3 for water mass definitions). The black lines are smoothed bathymetry contours every 1000 m.

of two boxes. Three sections extended from the Kerguelen Plateau, and the boxes were closed by a land boundary (Kerguelen Island) to the south and an east–west transect to the north of the plateau slopes. Figure 2 shows how the stations have been divided into transects and also shows the approximate locations of the fronts, based on a combination of their hydrographic definitions (Table 2) and the locations of the current jets detected by geostrophy, and by ADCP measurements. These front locations will be discussed further in section 4. The 60 full-depth stations were separated by an average distance of 36 km with finer sampling over steep topography and fronts.

[12] Station measurements included simultaneous CTD and lowered ADCP (LADCP) measurements. Microstructure observations are discussed by *Waterman et al*. [2012]. The CTD was a Sea-Bird 9/11 plus system with fin-mounted secondary sensors. Water samples were taken for salinity calibrations using a Guildline Autosal 8400B, calibrated using OSIL IAPSO standard seawater batch P149. Accuracies were 0.001 °C for temperature and 0.001 for salinity. Also mounted on the rosette was a Sea-Bird SBE-43 oxygen sensor. Samples were not analyzed for dissolved oxygen during the cruise so the instrument is uncalibrated, but the values are consistent with climatology (Orsi, A. H., and T. Whitworth III, WOCE Southern Ocean Atlas, http://woceSOatlas.tamu.edu) and reproducible for overlapping transects, so no drift was detected during the cruise. CTD data were processed using Sea-Bird software SBE Data Processing, Version 7.18, and binned into vertical profiles of 2 dbar average temperature, salinity, oxygen, and pressure.

[13] The LADCP package consisted of two RDI 300 kHz Workhorse ADCPs, though from station 16 onwards only one instrument (downward looking) was used. No LADCP data are available for stations 25 and 51. LADCP data were processed using software originating from Eric Firing's group at the University of Hawaii. The Visbeck software from Lamont-Doherty Earth Observatory (version 7b) was used for obtaining bottom tracked profiles. The bottom track profiles were used to confirm the output of the University of Hawaii software, but were otherwise not used. LADCP observations (averaged over the up and down cast) provided vertical profiles of 20 dbar average velocity. The LADCP profiles were detided using the ESR/OSU global inverse tide model TPXO7.2 [*Egbert and Erofeeva*, 2002]. The effects of detiding are small: the total transport through the region (see section 5) is estimated as 171 Sv without detiding or 174 Sv after detiding, but the error estimate of ±22 Sv is far greater than the difference caused by detiding.

[14] The underway water sampling system consisted of a Falmouth Scientific Ocean Temperature Module (OTM) measuring the SST at the water inlet, and a Falmouth Scientific OTM and Ocean Conductivity Module measuring temperature and conductivity in the wetlab. Two vessel-mounted ADCPs (VMADCPs) (75 kHz and 150 kHz Ocean Surveyors), controlled using the RDI VmDas software, version 1.42, were run throughout the survey. The data were processed to remove bad data (e.g., from interference, bubbles, outliers), and to remove the instrument misalignments. Results from the two VMADCPs are consistent with each other, and from now on, we use the data from the 75 kHz instrument, which can observe velocities down to approximately 800 m below the surface. The VMADCP profiles were similarly detided using the ESR/OSU global inverse tide model TPXO7.2 [*Egbert and Erofeeva*, 2002].

[15] Geostrophic shear between adjacent station pairs, relative to the deepest common level, was calculated from the CTD data. Velocities perpendicular to the cruise track from the LADCP and VMADCP velocities were used to adjust the geostrophic shear in order to calculate the total geostrophic transport. Station pairs were divided into two groups: deep pairs, where both stations were deeper than 1500 m; and shallow pairs, where at least one station was shallower than 1500 m. For deep pairs, the depth range was selected where the shears of the LADCP and geostrophic profiles were in closest agreement, which involved excluding depths below the deepest extent of the shallower station, and depths from the surface to between 300 and 600 m. Selection of the near-surface depth range to exclude was done heuristically. The offset between the geostrophic profile and the average of the two LADCP profiles was then used to adjust the geostrophic current. These offsets were confirmed by comparison with the VMADCP profiles between the two stations. For shallow pairs, depths from the surface to between 100 and 400 m were excluded, and offsets were calculated from the average of all the LADCP

and VMADCP profiles, including depths below the deepest extent of the shallower station. The station pairs with only one LADCP profile were treated in the same way as shallow station pairs. To join the end of the central transect to northern transect II (Figure 2), the "deep pair" process was also followed for stations 35 and 70, and stations 70 and 36.

[16] The transport through "bottom triangles" (the region below the deepest common level of two adjacent CTD stations where it is not possible to calculate geostrophic velocities directly) was calculated by extrapolating a constant geostrophic velocity below the deepest common level. Other methods were tested, such as extrapolating the geostrophic velocity gradient, or extrapolating the geopotential anomaly of the shallower station downwards [*Thompson and Heywood*, 2008]. Very little difference was found using these alternative methods since the currents are not bottom-intensified in this region. A constant velocity gradient assumption, for example, makes a difference of only 1 Sv to the 160 Sv transport of the combined SAF/STF (see section 4).

[17] The main source of uncertainty in the transport estimate is in determining the reference barotropic velocity from the ADCP data. The characteristic accuracy of the barotropic component of the ADCP flow, or, in other words, the uncertainty in referencing the geostrophic shear to the ADCP velocities, is 3 cm s^{-1} [*Thompson and Heywood*, 2008]. To estimate error bars, we apply random barotropic perturbations following a normal distribution with a standard deviation of 3 cm s^{-1} to individual velocity profiles. The error is then determined by calculating the rms deviation of 10,000 realizations of the resulting transport, and it is values calculated in this way which are quoted in sections 4 and 5.

[18] An 18 year time series, from January 1993 to December 2010, of absolute geostrophic velocities calculated from SSHs above geoid obtained by satellite altimetry, was acquired from Aviso (Archiving, Validation, and Interpretation of Satellite Oceanography). These are weekly gridded fields obtained on a 1/3° Mercator grid at 7 day intervals. The delayed-time (M)ADT "Ref" products are used: a homogeneous data set

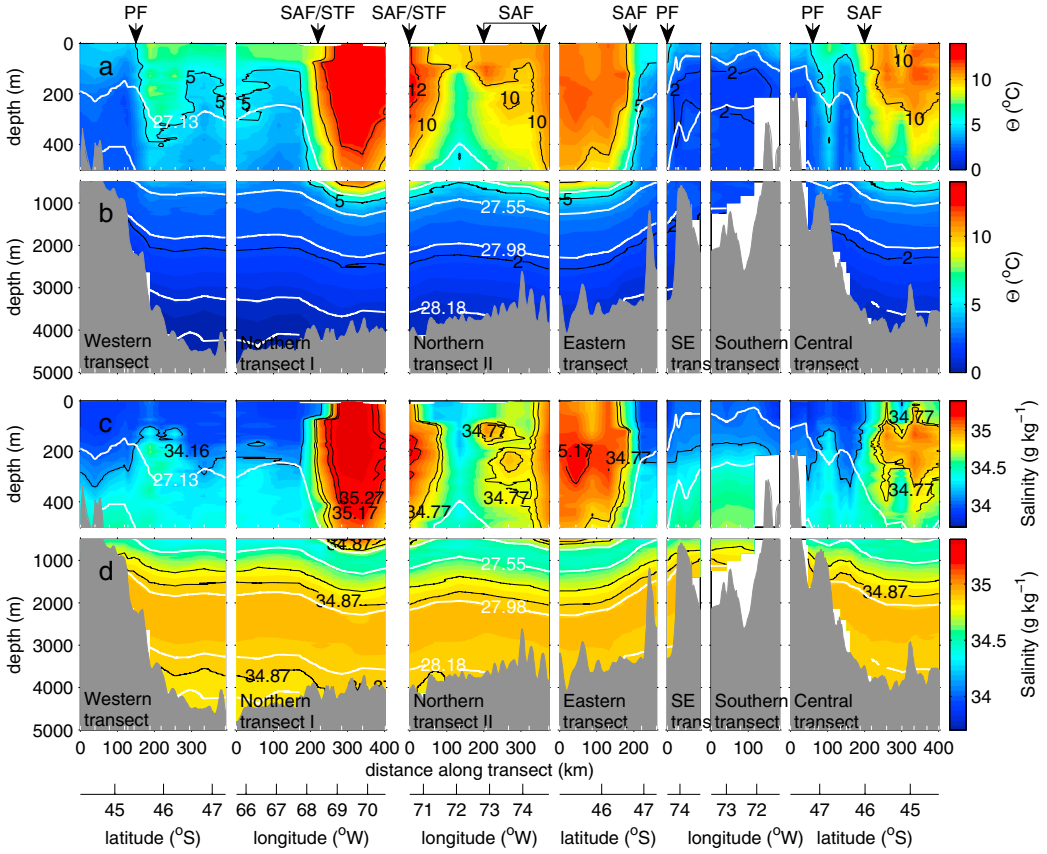

Figure 3. Temperature and salinity from the SOFine survey. Fields are displayed as a function of depth and along-transect distance, and the section as displayed starts in the southwestern corner of the survey domain, then runs clockwise along the rim of the region, and finally northeastward along the central transect. In all panels, neutral density contours (white) separate the water masses, according to the definitions in Table 3. White tickmarks along the lower axis show the station locations and the fronts are identified along the upper axis [Polar Front (PF), Subantarctic Front (SAF), Subtropical Front (STF)]. (a) Conservative temperature between 0 and 500 m depth. (b) Conservative temperature between 500 and 5000 m depth. In Figures 3a and 3b, black contours show temperatures of interest for frontal and water mass definitions (2, 5, 10, and 12 °C) according to the definitions in Tables 2 and 3. (c) Absolute salinity between 0 and 500 m depth. (d) Absolute salinity between 500 and 5000 m depth. In Figures 3c and 3d, black contours show salinities of interest for frontal and water mass definitions (34.16, 34.77, 34.87, 35.17, and 35.27 g kg^{-1}) according to the definitions in Tables 2 and 3.

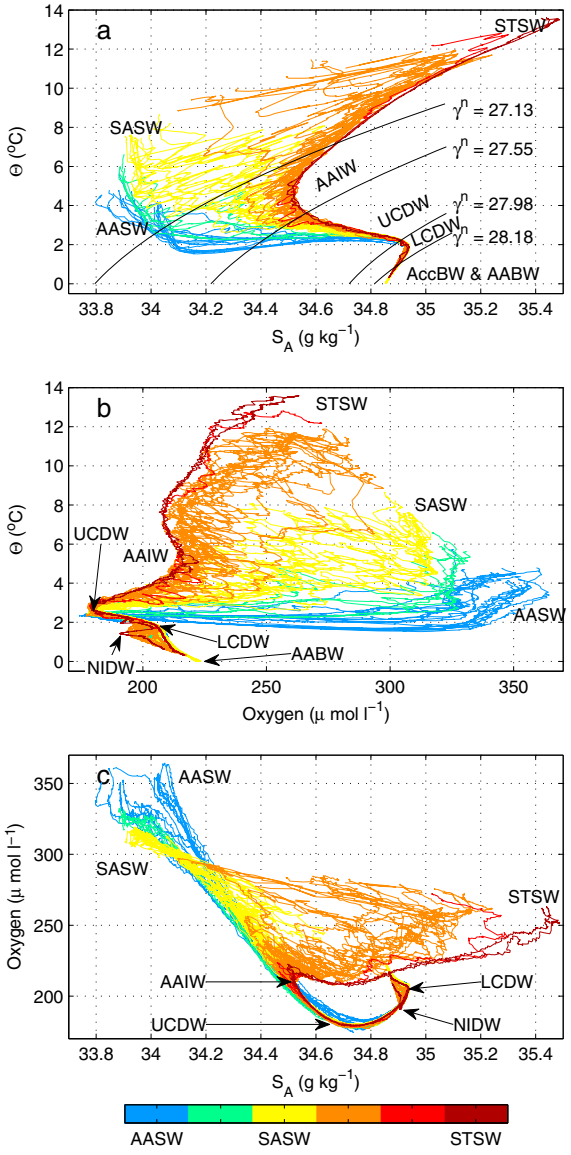

Figure 4. CTD (a)**Θ**–S_A, (b)**Θ**–oxygen, and (c) S_A–oxygen diagrams. The colors indicate the nature of the surface water (based on the average properties of the top 100 m): blue = AASW, green = intermediate properties between AASW and SASW, yellow = SASW, orange = intermediate properties between SASW and STSW, bright red = one station which had surface properties very close to STSW, except that it was slightly fresher, dark red = STSW (See Table 3 for water mass definitions).

based on two simultaneous satellite missions. These were used to produce weekly maps of geostrophic velocities in the SOFine survey region.

3. Water Masses

[19] The most voluminous density class found here is that of Lower Circumpolar Deep Water (LCDW) ($27.98<\gamma^n<28.18$, see Table 3), distinguished by a pronounced salinity maximum (Figures 3d and 4). In those parts of the central, eastern, and the two northern transects that lie to the north of, or within, the SAF (see Figure 2 and section 4 for front locations), water with the density of LCDW might more properly be labeled as North Indian Deep Water (NIDW) [*Gordon et al*., 1987], as is suggested by the low oxygen content (Figures 4b and 5b). NIDW is an aged form of North Atlantic Deep Water, characterized by a relatively low oxygen and high nutrient content, formed in the Indian Ocean basin. The particular hydrographic properties of NIDW are caused mainly by mineralization of organic matter [*van Aken et al*., 2004], unlike most major water masses which obtain their properties in the surface layers due to air–sea interaction. However, NIDW is usually treated as a separate water mass [*Warren*, 1981; *Park et al*., 1993; *You*, 2000; *van Aken et al*., 2004]. *Park et al*. [1993] observed NIDW between 66° and 77°E at 38°S, and between 75 and 77°E at 43–41°S, north of their reported position for the SAF/STF, and further north than observed in the SOFine survey. To our knowledge, this is the first observation of an injection of NIDW into the ACC on the northern flank of the Kerguelen Plateau. However, due to the scarcity of historical hydrographic data in this region, it would be premature to attribute this to a change in the deep circulation since it could simply be part of the natural climate variability.

[20] Below the LCDW layer, and seen predominantly in the deeper areas of the western and northern transect I, is a water mass with densities in the range $28.18<\gamma^n<28.27$. This layer lies below the salinity maximum of LCDW, but waters of this density class are referred to by a number of different names in different locations: generally Antarctic Bottom Water (AABW) in areas to the north of the ACC, Weddell Sea Deep Water within the Weddell Sea, and sometimes Modified CDW in areas to the south of the ACC (e.g., *Meijers et al*., 2010). We have chosen to designate this water mass as ACC bottom water (ACCbw) in line with *Orsi et al*. [1999]. At the bottom of the western transect and northern transect I, there is a thin layer of water with the density and salinity characteristics of AABW ($\gamma^n>28.27$, $S_A<34.9$ g kg^{-1}; Figure 3d), though it is slightly warmer (Figure 3b) and less oxygenated (Figure 5b) than required by the hydrographic definition (Table 3).

[21] Above the LCDW layer lies Upper Circumpolar Deep Water (UCDW) ($27.55<\gamma^n<27.98$), which has a pronounced oxygen minimum (Figure 4b and 5b). This water mass appears throughout the survey with fairly consistent salinity (Figure 3d) characteristics, but the temperature (Figure 3b) depends on the location relative to the PF. South of the PF (Figure 2), the UCDW layer is colder and considerably closer to the surface: ~300–1200 m instead of ~1000–2000 m to the north. Above the UCDW is a layer with the density ($27.13<\gamma^n<27.55$) of Antarctic Intermediate Water (AAIW). South of the SAF, this is considered part of the surface waters, but the steep isopycnals in Figure 3 show the subduction of this density class at the SAF. The subsurface salinity minimum characteristic of AAIW is clear north of the SAF, where the surface waters have high salinity (Figure 3d).

[22] The surface waters can be divided into broadly three types [*Park et al*., 1993]. STSW lies to the north of the SAF and is characterized by relatively high temperature and salinity (>12 °C, >35.27 g kg^{-1}) and low oxygen content (<270 μmol l^{-1}). SASW is characterized by lower temperatures and salinities (<9 °C, <34.16 g kg^{-1}) and higher oxygen content (>290 μmol l^{-1}) and lies between the PF and SAF. Antarctic Surface Water (AASW) is colder (<5 °C) and richer in oxygen (>315 μmol l^{-1}) and is found further south.

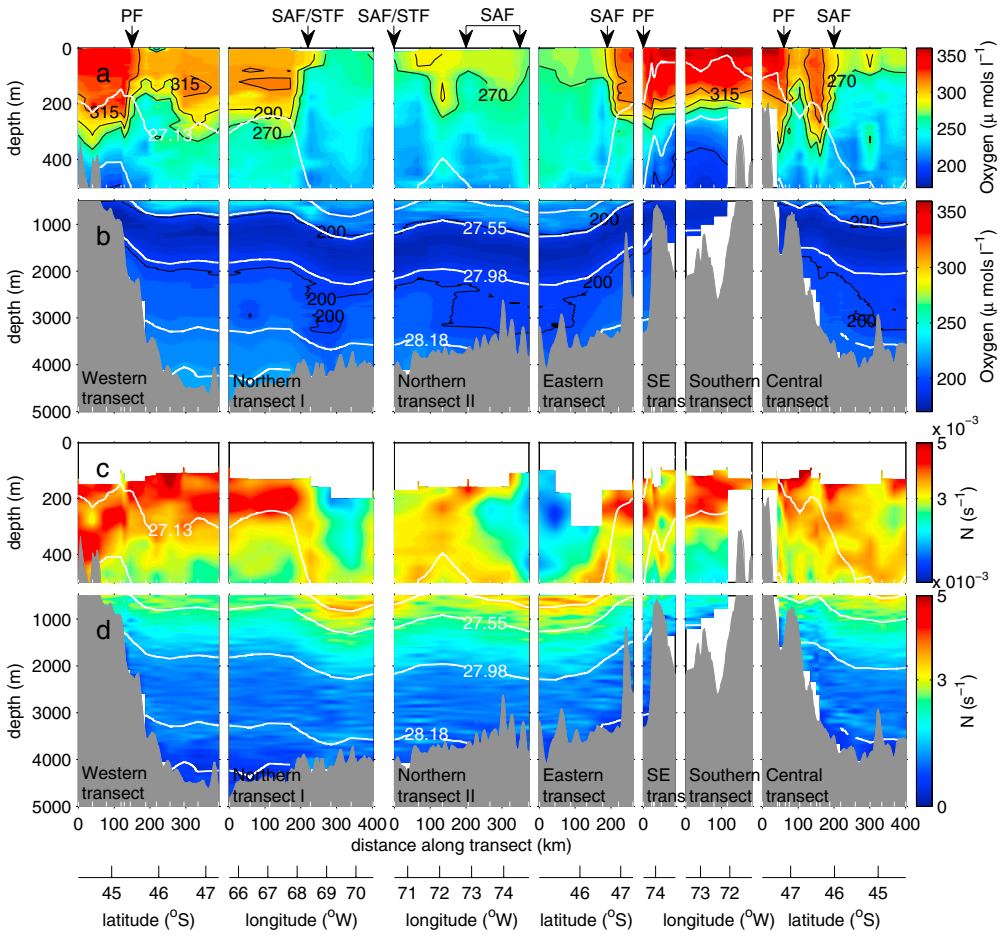

Figure 5. Dissolved oxygen and buoyancy frequency from the SOFine survey. This figure is laid out as in Figure 3. (a) Dissolved oxygen between 0 and 500 m depth. (b) Dissolved oxygen between 500 and 5000 m depth. In Figures 5a and 5b, black contours show concentrations of interest for water mass definitions (200, 270, 290, and 315 μ mol l^{-1}) according to the definitions in Table 3. (c) Smoothed buoyancy frequency (N) between 0 and 500 m depth. (d) Smoothed buoyancy frequency between 500 and 5000 m depth.

[23] The different surface water characteristics lead to particularly noticeable differences in the stratification of the near-surface waters. Figures 5c–d show the buoyancy frequency, smoothed by applying the adiabatic leveling method of *Bray and Fofonoff* [1981], with a pressure range of 100 db. North of the SAF, salinity and temperature increase towards the surface (but below the surface mixed layer) in a density-compensating manner, leading to weak stratification and a low buoyancy frequency in the STSW ($N \sim 1-2 \times 10^{-3}$ s^{-1}). At the base of this layer, the temperature decreases rapidly, but the decrease in salinity is no longer rapid enough to be density compensating (Figure 4), leading to a band of higher stratification ($N \sim 3-4 \times 10^{-3}$ s^{-1}) at a density of ~27.13 (Figures 5c–d), the boundary between AAIW and the surface waters. South of the SAF, salinity decreases while temperature increases towards the surface (below the surface mixed layer), leading to much higher stratification in the SASW and AASW ($N \sim 4-5 \times 10^{-3}$ s^{-1}).

4. Fronts and Transport

[24] A simplified schematic of the fronts and main water mass pathways is shown in Figure 6; for more detail, see Figure 2. A combined SAF/STF (Table 2) crosses the northern transects in a meander to the south and then to the north (Figures 2 and 6). This can be seen clearly in the sharp horizontal gradients in temperature and salinity (Figure 3: the transects cross the 10–12°C and 34.77–35.17 g kg^{-1} bands at 100 m, coincident with the rapid descent of the subsurface salinity minimum). These coincide with strong jets in the currents southward and then northward (Figures 7 and 8b), also seen in the surface geostrophic velocity fields derived from satellite altimetry (Figure 9). The sharp horizontal change across this front in surface temperature and salinity is also evident in Figure 7. However, we deduce from Figure 10 that not all the water that enters in this meander (160 ± 18 Sv between stations 25 and 31) leaves again to the north (103 ± 13 Sv between stations 31 and 34). Some of this water, with the surface water characteristics of SASW (Table 3 and Figure 2), is part of an eddy centered at approximately 70°E 43°S, seen clearly in the geostrophic velocity fields derived from satellite altimetry (Figure 9), particularly during the early weeks of the cruise. Thus, some of the 160 Sv entering between stations 25 and 31 travels west and leaves through the northern end of the western transect. We also surmise that some of the 160 Sv entering between

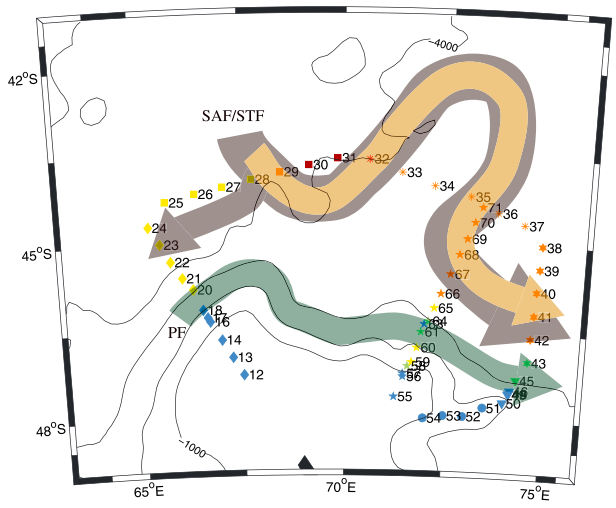

Figure 6. A simplified schematic of water mass pathways. Gray arrows show where all density classes are moving along the same pathway. The green arrow shows shallower waters only (UCDW, AAIW, and surface waters). The orange arrow shows NIDW. Station locations are shown as in Figure 2, with transects denoted by different symbols and colors representing different surface water properties. The thin black lines are smoothed bathymetry contours every 1000 m.

stations 25 and 31 continues to the east, rather than returning north. This is reasonably consistent with the transports through the central (99 ± 10 Sv between station 55 and 70) and eastern transects (135 ± 11 Sv between stations 38 and 46) being much greater than the transport through the western transect (33 ± 5 Sv from station 12 to 21, i.e., south of the westward flow associated with the eddy centered at approximately 70°E 43°S).

[25] Further east along northern transect II, a broad band of water enters the survey area heading southwest, seen in the velocity fields (Figures 7 and 8) and in the altimetry-derived geostrophic currents (Figure 9). The associated transport is 58 ± 14 Sv between stations 34 and 38 (Figure 10). Figure 3 shows a gradual descent of the subsurface salinity minimum across this transect, indicating that this is the SAF, and the surface waters have intermediate properties between SASW and STSW (Table 3 and Figure 2). 37 ± 10 Sv crosses northern transect II to the east of the central transect (stations 70 to 38) and 23 ± 10 Sv to the west (stations 34 to 70), in good agreement with the 58 Sv from stations 34 to 38.

[26] The altimetry-derived geostrophic currents (Figure 9) show the broad SAF entering the survey area across northern transect II becoming a narrower, faster flowing jet at around 71°E, 46°S (an area not covered by the hydrographic stations), particularly during the early weeks of the cruise. This jet then bends around to cross the central transect in a southeasterly direction and then the eastern transect flowing almost due east (particularly clear during the later weeks of the survey). This scenario, summarized in Figures 2 and 6, is consistent with the velocities recorded by the ADCPs (Figures 7 and 8), with the positions of the descent of the subsurface salinity minimum in Figure 3, and with the large transports across the central and eastern transects. The transport across the central transect between stations 63 and 70 (i.e., the SAF) is 85 ± 9 Sv (Figure 10). The sea surface salinity of the water crossing the central transect (Figure 7b) appears slightly fresher than in other jets which we consider to be the SAF, but we can see in Figure 3c that there is a thin fresher layer at the surface in these areas, with more saline water beneath. This could be due to surface Ekman drift pushing fresher water northward across the frontal zone.

[27] South of the SAF, another jet crosses the western and central transects (Figures 7 and 8a), becoming closer to the SAF as it travels east, until at the eastern transect there is no clear separation between the SAF and this more southern jet. We consider this to be the subsurface expression of the PF because the subsurface 2 °C isotherm is found in the S.E. and southern transects, just to the south of the location of this jet in the central and eastern transects (Figure 3a). The subsurface 2 °C isotherm is not present in the western transect and presumably is located further south. In all three of the western, central, and eastern transects, there is a rapid descent of isotherms near the location of this southernmost jet, as is commonly found in the vicinity of the PF, and cold, highly oxygenated surface waters with the properties of AASW lie

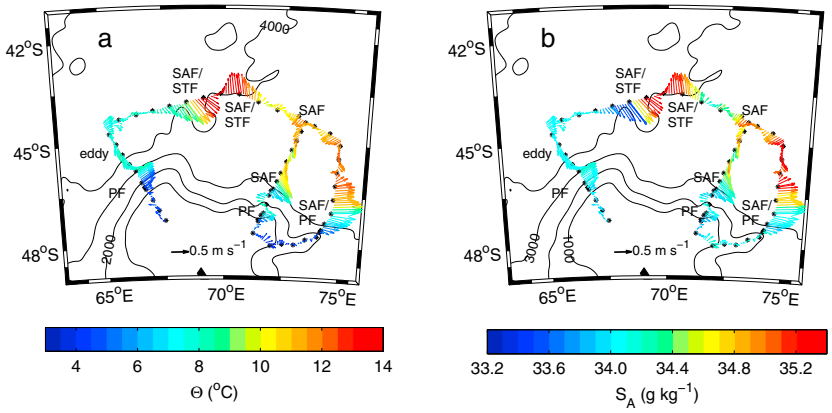

Figure 7. Current velocities observed by the 75 kHz VMADCP, averaged every 30 min, and over depths from 50 to 600 m where consistently good data was acquired. In Figure 7a, these are colored by the SST, in Figure 7b by the sea surface salinity (SSS) from the underway system. Front locations are indicated as follows: Polar Front (PF), Subantarctic Front (SAF), Subtropical Front (STF). The black lines are smoothed bathymetry contours every 1000 m.

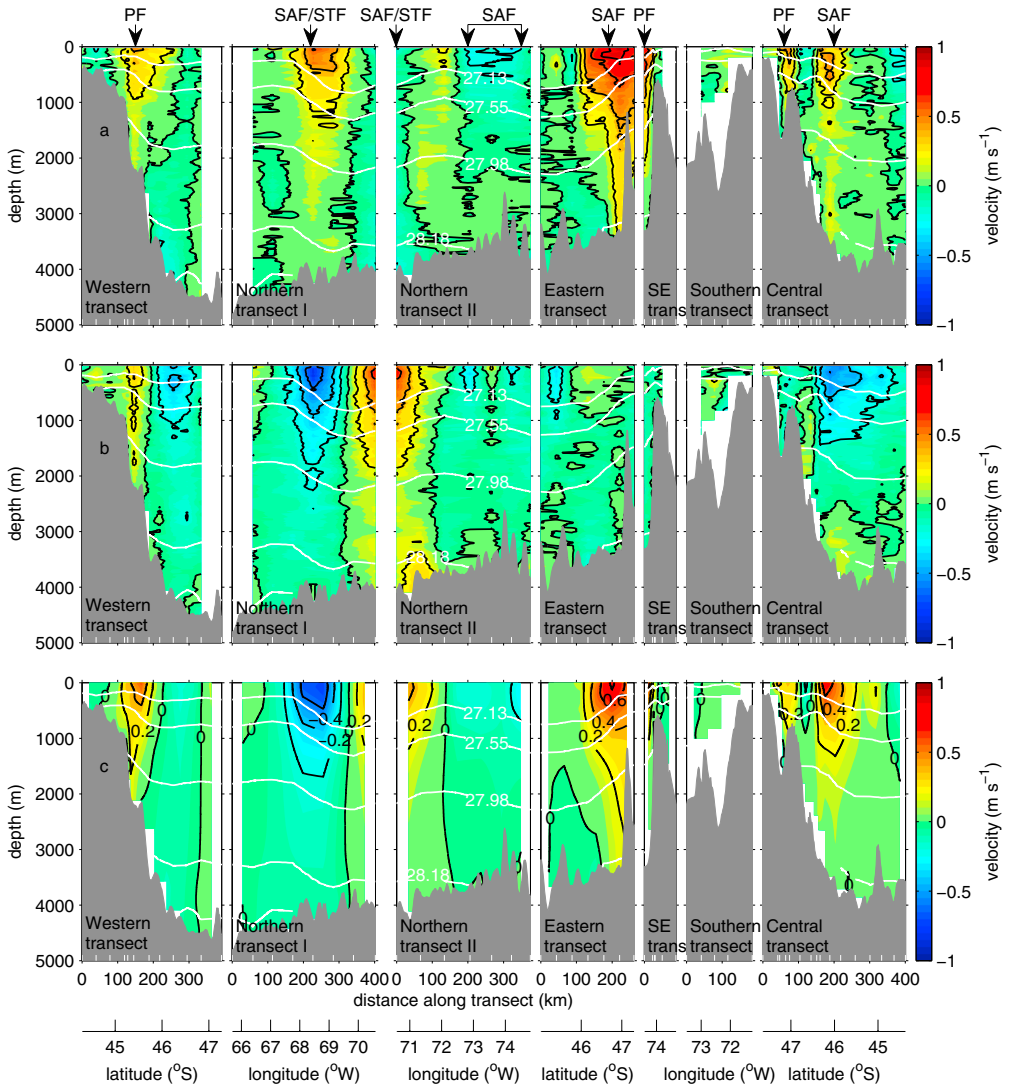

Figure 8. (a) Eastward and (b) northward LADCP velocity, and (c) cross-track geostrophic velocity, referenced to the LADCP velocities (all m s^{-1}, color). Fields are displayed as a function of depth and along-transect distance, and the section as displayed starts in the southwestern corner of the survey domain, then runs clockwise along the rim of the region, and finally northeastward along the central transect. In all panels, neutral density contours (white) separate the water masses, according to the definitions in Table 3. White tickmarks along the lower axis show the station locations and the fronts are identified along the upper axis [Polar Front (PF), Subantarctic Front (SAF), Subtropical Front (STF)].

to the south (Table 3 and Figure 2). Overall, this seems consistent with a northern branch of the PF, such as those found by *Sokolov and Rintoul* [2009] and *Holliday and Read* [1998]. In the SOFine study region, we do not find the surface expression of the PF, which was placed to the north of the Kerguelen Plateau by *Orsi et al.* [1995].

[28] Crossing the western transect the transport of the PF between stations 12 and 21 is 33 ± 5 Sv (Figure 10). Crossing the central transect, the PF is associated with a transport of 14 ± 3 Sv between stations 55 and 63, although the rapid reversal in current direction (westward between the jets we associate with the PF and SAF) suggests that there may also be a small eddy in this region, making it difficult to accurately estimate the transport of a particular jet. In the eastern transect, it is not possible to separate the SAF and PF. Overall, it is difficult to estimate the transport of the PF due to the merging of the fronts and presence of eddies, but it seems likely that it is more than zero, as was reported by *Park et al.* [1993, 2008b, 2009].

[29] The altimetry-derived geostrophic currents do not always entirely agree with the currents found by the SOFine survey, particularly in the shallower areas of the survey region, and thus the jets we associate with the PF are not evident in Figure 9. A possible explanation for this discrepancy is that the resolution of the gridded altimetric dataset is 1/4°, considerably coarser than the station spacing over the continental slope where the PF jets are found. We also suggest that both the tide model and the geoid (used in the calculation of absolute geostrophic velocity from SSH measurements) may be less accurate over the continental slope and shelf than in deep waters. *Griesel et al.* [2012] compare four Mean Dynamic Ocean Topography (MDT) products, in which the geoid is a major source of uncertainty. They find

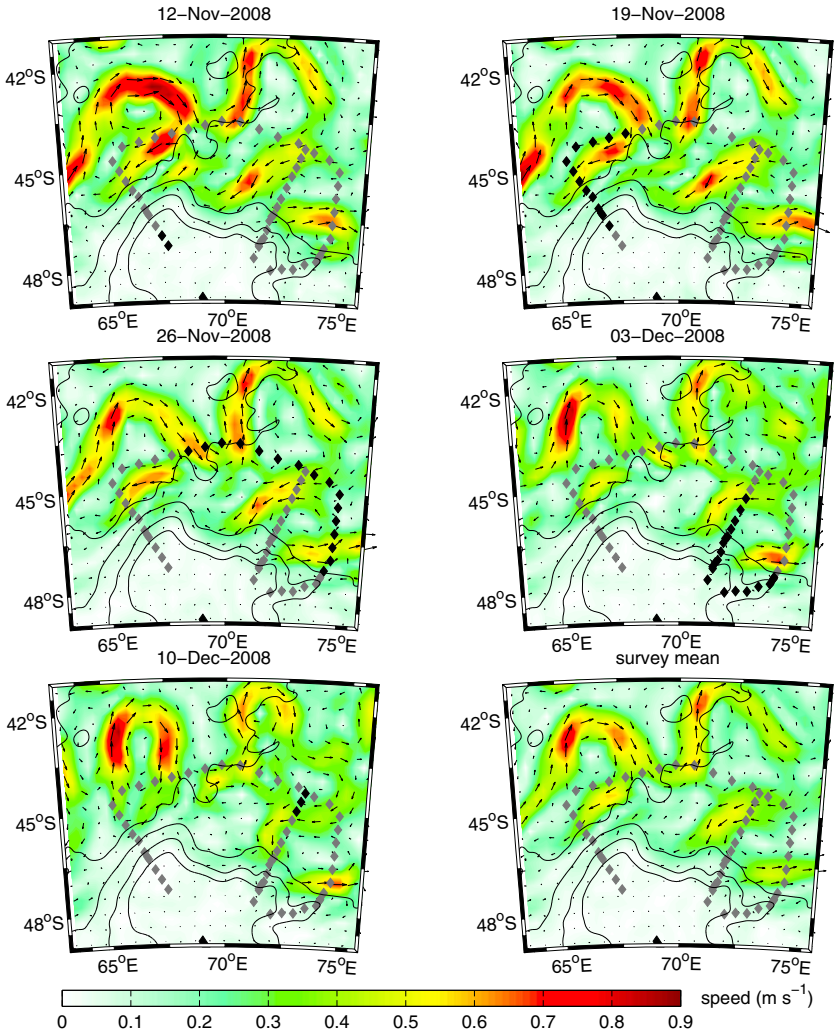

Figure 9. Geostrophic currents (black arrows) from satellite altimetry, with current speed in color. These are the merged-satellites, gridded, absolute geostrophic velocities produced by Aviso. The black lines are smoothed bathymetry contours every 1000 m. Diamonds show the station locations, with the stations occupied during the week represented by each altimetry map in black, and the other stations in gray.

that the standard deviation of the four products reaches ≥20 cm in localized areas where MDT gradients are high and the surface flow is restricted by topography, such as near the Kerguelen Plateau.

[30] The altimetry-derived geostrophic currents in the deeper (northern) parts of the survey region are in good agreement with the currents observed in the SOFine survey. Altimetry-derived geostrophic currents from January 1993 to December 2010 show that the currents observed in the northern parts of the SOFine survey region are typical for this area. Large meanders and eddies are a persistent feature, though their precise location varies. This is further supported by eddy kinetic energy maps such as those discussed by *Sallee et al*. [2008] and *Trani et al*. [2011], which show a relative maximum in eddy kinetic energy in the region of the Kerguelen Plateau. Unsteady jet behavior involving persistent jet formation and merging has been linked to interactions with eddies and topography [*Thompson*, 2008; *Thompson et al*., 2010; *Thompson and Richards*, 2011]. In particular, *Thompson* [2010] demonstrate that topography does not simply steer jets in a passive manner, but can generate a range of patterns of unsteady jet behavior through modification of the mean flow and of local potential vorticity gradients and the subsequent feedback on baroclinic instability. Figure 11a shows a broad band of high mean current speed across the northern part of the survey region, coincident with the location of the STF/SAF observed in the SOFine survey, and with the main jets in other hydrographic surveys [*Park et al*., 1993; *Sparrow et al*., 1996]. The currents in this band are also the most highly variable in the survey region, evidenced by the high standard deviation of the speed (Figure 11b). In the eastern part of this region, the currents in this band are slower and less variable. *Moore et al*. [1999] noted that large-scale meandering of fronts was inhibited near large topographic features because of the large gradients in planetary potential vorticity, which is consistent with the reduced variability in current speed observed as the main jet encounters the Kerguelen Plateau.

5. Total Transport Through the Region

[31] The baroclinic transport (i.e., calculated assuming a level of no motion at the deepest common level) through this

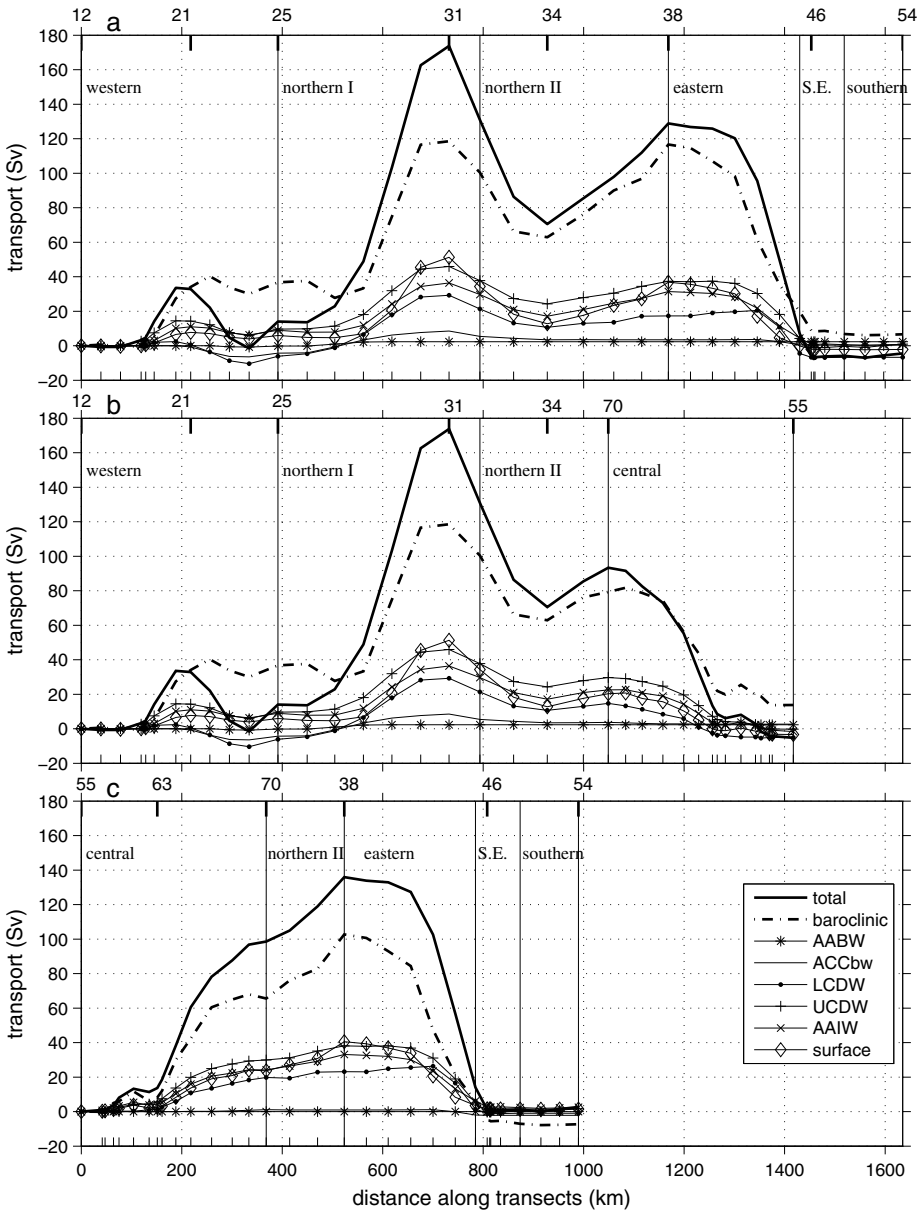

Figure 10. Transport of different water masses, summed over depth, around the three boxes formed by the survey. It is assumed that there is zero net transport over the shallow topography between the southernmost ends of the western and central transects. (a) The largest box from the western to the eastern transect, with the southern boundary partially closed by the southern transect, and partially by the above assumption. (b) The western box from the western to the central transect, with the southern boundary closed by the above assumption. (c) The eastern box from the central to the eastern transect, which is closed by the southern transect. All station locations are marked as ticks along the lower axis, with particular stations which are used to separate fronts marked on the upper axis. The dash-dot line in all three plots is the transport relative to the deepest common level.

region is 119 Sv (cumulative transport from station 12 to station 31), comparable with the baroclinic transports found by *Park et al.* [1993] and *Sparrow et al.* [1996] of ~100 and 110 Sv, respectively. The total transport through this region is 174 ± 22 Sv (cumulative transport from station 12 to station 31). An alternative, "worst case" scenario for estimating the error is obtained following *Gordon et al.* [2001] by assuming that all the LADCP profiles are systematically biased by $1\,\mathrm{cm\,s^{-1}}$. This yields an error estimate of ± 39 Sv for the total transport between stations 12 and 31. The presence of the large eddy centered at approximately 70°E 43°S does not affect the total transport, because water associated with this eddy which enters the box across northern transect I also leaves the box across the northern end of the western transect.

[32] At first glance, 174 Sv might seem rather large when compared with other ACC transport measurements, but in the SOFine region, the transport associated with the ACC may be augmented by the ~15 Sv of the Indonesian Throughflow [*Sprintall et al.*, 2009] as it returns eastward. Moreover,

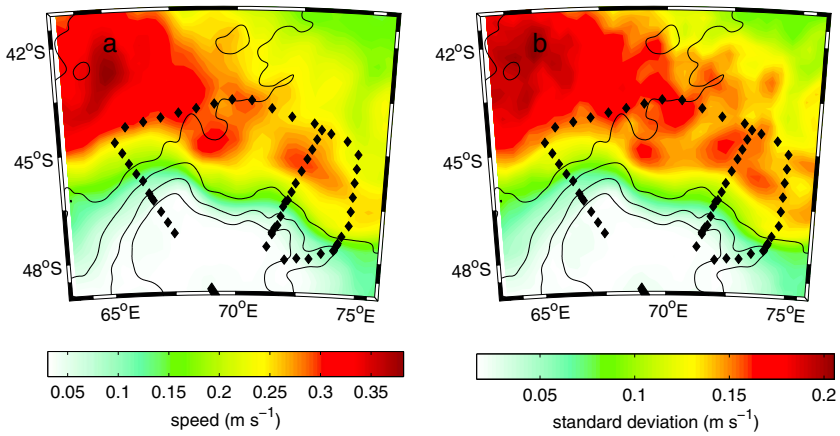

Figure 11. Altimetry-derived geostrophic currents from 1992 to 2010. The black lines are smoothed bathymetry contours every 1000 m, and the black diamonds are the station locations. (a) Mean speed and (b) standard deviation of the speed.

we are not, in fact, measuring the transport of the ACC, since our survey encompasses the STF, which does not pass through Drake Passage, and does not cover the whole PF, nor the SACCF or SB. In addition, the SOFine survey is one snapshot measurement of a variable system and may not be entirely representative of the long-term average. Several authors have shown that the barotropic component of the total transport can have high temporal variability (e.g., *Cunningham et al.* [2003]), although the altimetric observations suggest that the values found during the SOFine survey are unlikely to be significantly atypical.

[33] The total cumulative transport between station 12 and station 31 of each water mass is shown in Figure 12, with transport in neutral density layers. We compare these with the baroclinic transport of *Rintoul and Sokolov* [2001] calculated for five repeat sections along SR3 from Tasmania to Antarctica (their Plate 2), and the baroclinic and total transport found by *Cunningham et al.* [2003] for three repeat sections along SR1 across Drake Passage (their Tables 3 and 4). In the SOFine survey region, the total eastward transport of surface waters ($\gamma^n < 27.13$) is 51 Sv, far greater than that observed by *Cunningham et al.* [2003] in Drake Passage. The STF does not pass through Drake Passage, and we see in Figure 10 that much of this surface water transport is associated with the combined STF/SAF, so the difference between this region and Drake Passage is not surprising. However, the baroclinic transport of water with $\gamma^n < 27.13$, 45 Sv, is also significantly greater than that found by *Rintoul and Sokolov* [2001], whose survey does cross the STF. This may be partially due to the westward transport of light waters by the Tasman Outflow, offsetting some of the eastward transport of the STF, but we also speculate that some of this surface water may recirculate within the Indian Ocean basin.

[34] The transport of AAIW and the lighter UCDW layers ($27.13 < \gamma^n < 27.8$) is broadly similar in all three regions (SR1, SR3, and the SOFine survey region), and across the various years of observation, with around 8–12 Sv for every 0.1 kg m^{-3}. In all three regions, the transport of water with γ^n in the range 27.8–28.2 is larger than other density layers and particularly large in 1997 and 2000 in Drake Passage

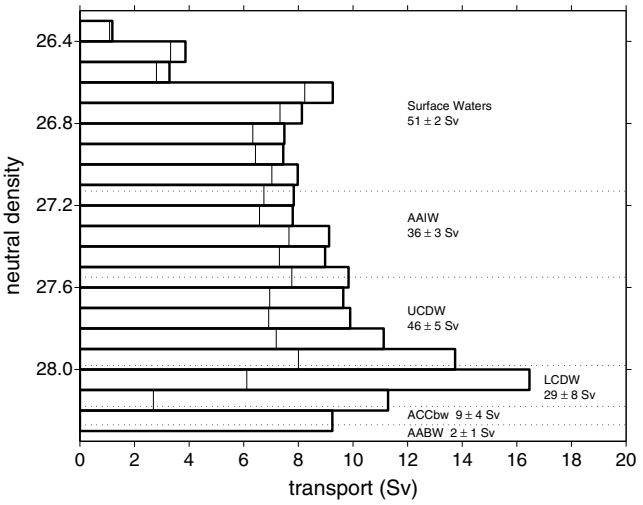

Figure 12. Transport in neutral density layers, summed from station 12 to station 31. The thick line is the total transport, the thinner line is the baroclinic transport. In the lightest density layer, the baroclinic transport is hard to distinguish from the total because they are both 1 Sv. In the densest layer, the baroclinic transport is zero. Dashed lines indicate water mass boundaries.

Table 4. Cumulative Transport of Each Water Mass From Station 12 to Station 54

Water Mass	Total Transport (Sv)
AABW	2 ± 2
ACCbw	0 ± 4
LCDW	-7 ± 12
UCDW	1 ± 8
AAIW	1 ± 4
SW	-2 ± 4
Total	-4 ± 31

(74 and 93 Sv total transport respectively, compared with 53 Sv (total), 24 Sv (baroclinic), in the SOFine region (Figure 12)). Since the surface expression of the PF, plus the SACCF and SB, passes through Drake Passage, it is not surprising that greater volumes of dense water are found in Drake Passage than in the SOFine survey region, which does not encompass those fronts. In Drake Passage, water with γ^n in the range 27.8–28.2 also displays the greatest barotropic component (with which our results agree), and the greatest temporal variability in the total transport [*Cunningham et al.*, 2003]. *Rintoul and Sokolov* [2001] found larger baroclinic transports of LCDW than in the present study or in the results of *Cunningham et al.* [2003], and less temporal variability in the baroclinic transport of denser waters than lighter, but it is unknown whether either finding is true of the total transport across SR3.

[35] For water with $\gamma^n > 28.2$, the baroclinic transports observed by *Cunningham et al.* [2003] and *Rintoul and Sokolov* [2001] are broadly consistent with each other, though much greater than observed here since the surface PF, SACCF, and SB pass the Kerguelen Plateau to the south of the SOFine survey region. The total transport of water with $\gamma^n > 28.2$ we observe (9 Sv) is well within the temporal variability of the total transport observed in Drake Passage.

[36] An alternative way of considering the transport of AABW is to consider the transport of deep water with a potential/conservative temperature less than 0 °C, instead of water with a particular density. We do not observe any

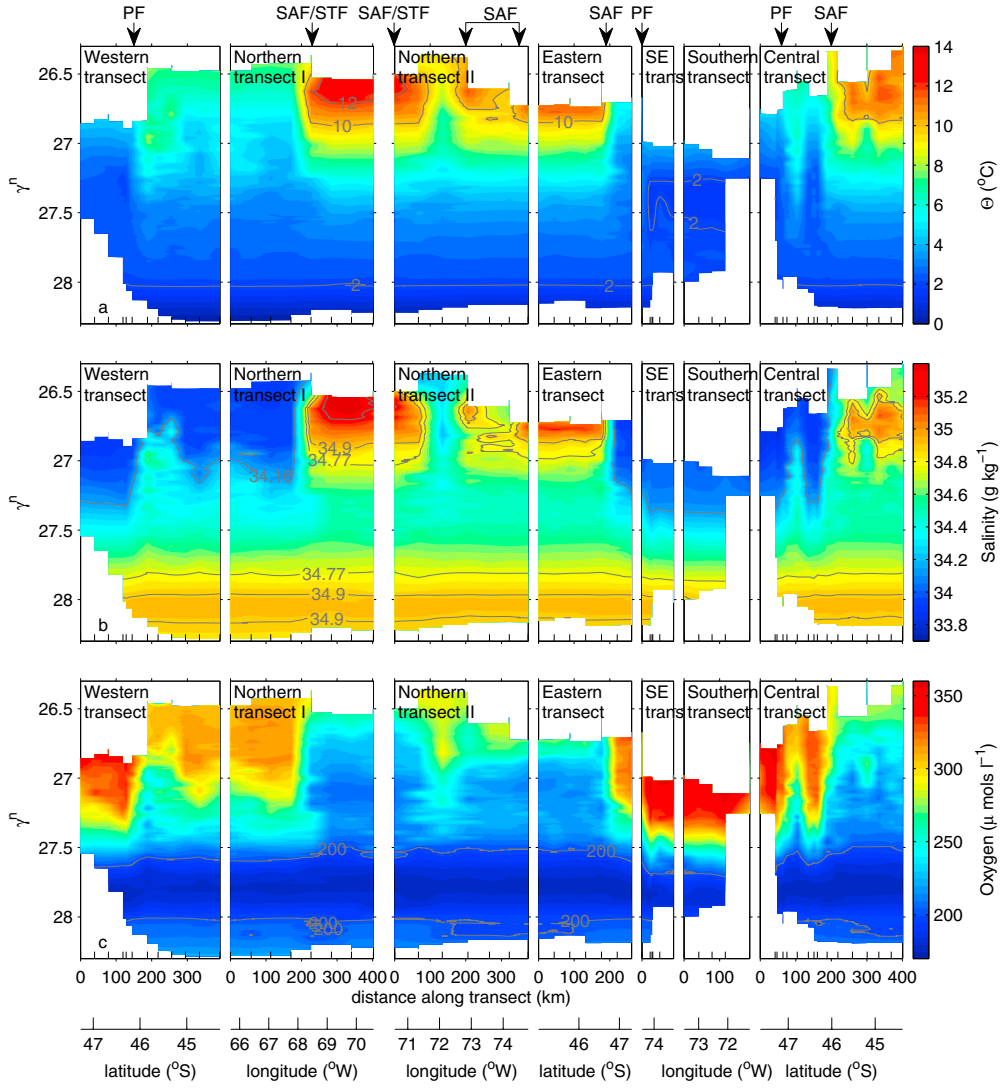

Figure 13. Temperature, salinity, and dissolved oxygen against neutral density. In all panels, black tickmarks along the lower axis show the station locations, and the fronts are identified along the upper axis [Polar Front (PF), Subantarctic Front (SAF), Subtropical Front (STF)]. (a) Conservative temperature. Gray contours show the temperatures of interest for frontal definitions (2 °C, 10 °C, and 12 °C) according to the definitions in Table 2. (b) Absolute salinity. Gray contours show some of the salinities of interest for frontal and water mass definitions (34.16, 34.77, 34.9, and 35.27 g kg^{-1}) according to the definitions in Tables 2 and 3. (c) Dissolved oxygen. Gray contours show where the concentration is $<200\,\mu$mol l^{-1}, indicating the presence of UCDW (Table 3).

water with a conservative temperature less than 0 °C. *Park et al*. [2009] do not report any water with a potential temperature less than 0 °C passing through the FT. *Heywood et al*. [1999] report a net westward transport of water with a potential temperature less than 0 °C of ~17 Sv passing through the PET. While these studies were all based on different datasets and were taken at different times, collectively they suggest that there is no net eastward transport of AABW (by that definition) at these longitudes. It is only by using a density-based definition that we find net eastward transport of AABW of 2 ± 1 Sv, and that is more than offset by the westward transport through the PET reported by *Heywood et al*. [1999].

6. Vertical and Horizontal Exchange

[37] The net transport around all three of the boxes formed by the survey is close to zero (Figure 10), indicating that it was reasonable to assume zero net transport over the shallow topography between the southernmost ends of the western and central transects. The net transport of each water mass is also zero (Table 4) within the estimated errors, indicating that no substantial diapycnal water mass transformation is required to close the transport budget. This is perhaps somewhat surprising as one might have expected this to be a region of high mixing given the bathymetric slopes and close proximity of major jets. *Waterman et al*. [2012] use centimeter-scale shear measured by a microstructure profiler to calculate turbulent dissipation. They find that the enhancement of turbulent dissipation at depth, in association with ACC jets flowing over small-scale topography in the SOFine study region, is not as pronounced as expected from past fine-scale parameterization studies and lee wave radiation calculations. They suggest that this may be due in part to the modest small-scale topographic roughness in the SOFine region, but also that a nonlocal balance applies: the energy generated propagates away and is deposited elsewhere, possibly due to internal wave-mean flow interactions.

[38] *Bower et al*. [1985] assessed the ability of the Gulf Stream to act as a "barrier" or "blender" to transport by contouring water properties against potential density instead of pressure. Plots of conservative temperature, absolute salinity, and dissolved oxygen against neutral density (Figure 13) show strong horizontal gradients across isopycnals corresponding to surface waters ($\gamma^n < 27.13$) at front locations indicating that the fronts act as barriers to transport within this density range. Deeper in the water column, for isopycnals characteristic of AAIW and UCDW ($27.13 < \gamma^n < 27.98$), the property gradients become weaker, suggesting that the fronts may be weak barriers or even blenders. Deeper still, for LCDW, ACCbw, and AABW ($\gamma^n > 27.98$), properties are almost entirely homogeneous on isopycnals (apart from the low oxygen signature of NIDW) indicating that these water masses are well mixed across fronts.

7. Conclusions

[39] We have presented a high-resolution hydrographic survey carried out on the northern flank of the Kerguelen Plateau. We identified a complex meandering current system with a blended STF/SAF to the north, a subsurface expression of the PF to the south, and a blended SAF/PF to the east, summarized as a schematic in Figure 2. An 18 year time series of surface geostrophic currents from satellite altimetry shows that the meanders and eddies observed during this survey are typical of the region, though the exact location of such features varies. The eastward baroclinic transport referenced to the deepest common level is 119 Sv, consistent with previous estimates in this region. The total eastward volume transport in the region is 174 ± 22 Sv, considerably larger than previous baroclinic estimates because of the large barotropic component of the total flow, but still broadly consistent with other estimates of transport in the Indian Ocean (Figure 1). Most of this transport is associated with the blended STF/SAF. It proved difficult to estimate the transport of the subsurface PF due to the merging of the fronts and presence of eddies, but our results suggest a transport between 14 and 33 Sv. The fronts act as barriers to the exchange of water mass properties across surface waters, but may be acting as blenders deeper in the water column. Significant water mass transformation across isopycnals is not required to balance the budgets in this region. To our knowledge, we identify for the first time the presence of NIDW in the ACC on the northern flank of the Kerguelen Plateau.

[40] This study has highlighted the complexity of the circulation in the Kerguelen region. The study presented here, as that discussed by *Park et al*. [1993], was a snapshot of the circulation at a particular time. One remaining question is the representativeness of such surveys in such a highly variable domain. Although altimetric currents are promising in deep water, they are currently not accurate over the continental slope and shelf. Future efforts could focus on repeat hydrographic measurements, perhaps incorporating data from autonomous vehicles such as gliders and floats.

[41] **Acknowledgments.** The SOFine project is funded by the U.K.'s Natural Environmental Research Council (NE/G001510/1 and NE/B503717). We thank all the scientists, technicians, officers, and crew involved in JC029. A Natural Environment Research Council PhD studentship at UEA supported G.M.D. during the analysis and writing of this report. The altimeter products were produced by Ssalto/Duacs and distributed by Aviso, with support from Cnes (http://www.aviso. oceanobs.com/duacs/).

References

Bower, A. S., H. T. Rossby, and J. L. Lillibridge (1985), The Gulf Stream - barrier or blender?, *J. Phys. Oceanogr.*, *15*(1), 24–32.

Bray, N. A., and N. P. Fofonoff (1981), Available potential-energy for mode eddies, *J. Phys. Oceanogr.*, *11*(1), 30–47.

Charrassin, J. B., Y. H. Park, Y. Le Maho, and C. A. Bost (2004), Fine resolution 3D temperature fields off Kerguelen from instrumented penguins, *Deep Sea Res.*, *51*(12), 2091–2103.

Cunningham, S. A., S. G. Alderson, B. A. King, and M. A. Brandon (2003), Transport and variability of the Antarctic Circumpolar Current in Drake Passage, *J. Geophys. Res.*, *108*(C5), 8084.

Deacon, G. E. R. (1937), The hydrology of the Southern Ocean, *Discovery Reports*, *15*, 1–124.

Egbert, G. D., and S. Y. Erofeeva (2002), Efficient inverse modeling of barotropic ocean tides, *J. Atmos. Oceanic Technol.*, *19*(2), 183–204.

Ganachaud, A., C. Wunsch, J. Marotzke, and J. Toole (2000), Meridional overturning and large-scale circulation of the Indian Ocean, *J. Geophys. Res.*, *105*(C11), 26,117–26,134.

Gladyshev, S., M. Arhan, A. Sokov, and S. Speich (2008), A hydrographic section from South Africa to the southern limit of the Antarctic Circumpolar Current at the Greenwich Meridian, *Deep Sea Res.*, *55*(10), 1284–1303.

Gordon, A. L., J. R. E. Lutjeharms, and M. L. Grundlingh (1987), Stratification and circulation at the Agulhas Retroflection, *Deep Sea Res.*, *34*(4), 565–599.

Gordon, A. L., M. Visbeck, and B. Huber (2001), Export of Weddell Sea Deep and Bottom Water, *J. Geophys. Res.*, *106*(C5), 9005–9017.

Griesel, A., M. R. Mazloff, and S. T. Gille (2012), Mean dynamic topography in the Southern Ocean: Evaluating Antarctic Circumpolar Current transport, *J. Geophys. Res.*, *117*, C01020.

Heywood, K. J., and B. A. King (2002), Water masses and baroclinic transports in the South Atlantic and Southern oceans, *J. Mar. Res.*, *60*(5), 639–676.

Heywood, K. J., M. D. Sparrow, J. Brown, and R. R. Dickson (1999), Frontal structure and Antarctic Bottom Water flow through the Princess Elizabeth Trough, Antarctica, *Deep Sea Res.*, *46*(7), 1181–1200.

Holliday, N. P., and J. F. Read (1998), Surface oceanic fronts between Africa and Antarctica, *Deep Sea Res.*, *45*(2-3), 217–238.

IOC, SCOR, and IAPSO, (2010), The international thermodynamic equation of seawater - 2010: Calculations and use of thermodynamic properties, Intergovernmental Oceanographic Commission, Manuals and Guides No. 56, UNESCO (English).

Jackett, D. R., and T. J. McDougall (1997), A neutral density variable for the world's oceans, *J. Phys. Oceanogr.*, *27*(2), 237–263.

McDonagh, E. L., H. L. Bryden, B. A. King, and R. J. Sanders (2008), The circulation of the Indian Ocean at 32 degrees S, *Prog. Oceanogr.*, *79*(1), 20–36.

Meijers, A. J. S., A. Klocker, N. L. Bindoff, G. D. Williams, and S. J. Marsland (2010), The circulation and water masses of the Antarctic shelf and continental slope between 30 and 80 degrees E, *Deep Sea Res.*, *57*(9-10), 723–737.

Moore, J. K., M. R. Abbott, and J. G. Richman (1999), Location and dynamics of the Antarctic Polar Front from satellite sea surface temperature data, *J. Geophys. Res.*, *104*(C2), 3059–3073.

Naveira Garabato, A. C. (2009), RRS James Cook Cruise 29, 01 Nov-22 Dec 2008. SOFine Cruise Report: Southern Ocean Finestructure. National Oceanography Centre Southampton Cruise Report No. 35, 216 pp.

Olbers, D., V. Gouretski, G. Seiss, and J. Schroter (1992), Hydrographic Atlas of the Southern Ocean, Alfred Wegener Inst. for Polar and Mar. Res., Bremerhaven, Germany.

Orsi, A. H., T. Whitworth, and W. D. Nowlin (1995), On the meridional extent and fronts of the Antarctic Circumpolar Current, *Deep Sea Res.*, *42*(5), 641–673.

Orsi, A. H., G. C. Johnson, and J. L. Bullister (1999), Circulation, mixing, and production of Antarctic Bottom Water, *Prog. Oceanogr.*, *43*(1), 55–109.

Park, Y. H., L. Gamberoni, and E. Charriaud (1993), Frontal structure, water masses, and circulation in the Crozet Basin, *J. Geophys. Res.*, *98*(C7), 12,361–12,385.

Park, Y. H., E. Charriaud, P. Craneguy, and A. Kartavtseff (2001), Fronts, transport, and Weddell Gyre at 30 degrees E between Africa and Antarctica, *J. Geophys. Res.*, *106*(C2), 2857–2879.

Park, Y. H., F. Roquet, I. Durand, and J. L. Fuda (2008a), Large-scale circulation over and around the Northern Kerguelen Plateau, *Deep Sea Res.*, *55*(5-7), 566–581.

Park, Y. H., N. Gasco, and G. Duhamel (2008b), Slope currents around the Kerguelen Islands from demersal longline fishing records, *Geophys. Res. Lett.*, *35*(9), L09604.

Park, Y. H., F. Vivier, F. Roquet, and E. Kestenare (2009), Direct observations of the ACC transport across the Kerguelen Plateau, *Geophys. Res. Lett.*, *36*, L18603.

Rintoul, S. R., and S. Sokolov (2001), Baroclinic transport variability of the Antarctic Circumpolar Current south of Australia (WOCE repeat section SR3), *J. Geophys. Res.*, *106*(C2), 2815–2832.

Roquet, F., Y. H. Park, C. Guinet, F. Bailleul, and J. B. Charrassin (2009), Observations of the Fawn Trough Current over the Kerguelen Plateau from instrumented elephant seals, *J. Mar. Syst.*, *78*(3), 377–393.

Sallee, J. B., K. Speer, R. Morrow, and R. Lumpkin (2008), An estimate of Lagrangian eddy statistics and diffusion in the mixed layer of the Southern Ocean, *J. Mar. Res.*, *66*, 441–463.

Sievers, H. A., and W. D. Nowlin (1984), The stratification and water masses at Drake Passage, *J. Geophys. Res.*, *89*(NC6), 489–514.

Smith, I. J., D. P. Stevens, K. J. Heywood, and M. P. Meredith (2010), The flow of the Antarctic Circumpolar Current over the North Scotia Ridge, *Deep Sea Res.*, *57*, 14–28.

Smith, W. H. F., and D. T. Sandwell (1997), Global sea floor topography from satellite altimetry and ship depth soundings, *Science*, *277*(5334), 1956–1962.

Sokolov, S., and S. R. Rintoul (2007), Multiple jets of the Antarctic Circumpolar Current south of Australia, *J. Phys. Oceanogr.*, *37*(5), 1394–1412.

Sokolov, S., and S. R. Rintoul (2009), Circumpolar structure and distribution of the Antarctic Circumpolar Current fronts: 1. Mean circumpolar paths, *J. Geophys. Res.*, *114*, C11018.

Sparrow, M. D., K. J. Heywood, J. Brown, and D. P. Stevens (1996), Current structure of the south Indian Ocean, *J. Geophys. Res.*, *101*(C3), 6377–6391.

Sprintall, J., S. E. Wijffels, R. Molcard, and I. Jaya (2009), Direct estimates of the Indonesian Throughflow entering the Indian Ocean: 2004-2006, *J. Geophys. Res.*, *114*, C07001.

Thompson, A. F. (2008), The atmospheric ocean: eddies and jets in the Antarctic Circumpolar Current, *Philos. Trans. R. Soc. London*, *366*(1885), 4529–4541, doi:10.1098/rsta.2008.0196.

Thompson, A. F. (2010), Jet formation and evolution in baroclinic turbulence with simple topography, *J. Phys. Oceanogr.*, *40*(2), 257–278, doi:10.1175/2009JPO4218.1.

Thompson, A. F., and K. J. Heywood (2008), Frontal structure and transport in the northwestern Weddell Sea, *Deep-Sea Res.*, *55*(10), 1229–1251.

Thompson, A. F., and K. J. Richards (2011), Low frequency variability of Southern Ocean jets, *J. Geophys. Res.*, *116*, C09022, doi:10.1029/2010JC006749.

Thompson, A. F., P. H. Haynes, C. Wilson, and K. J. Richards (2010), Rapid Southern Ocean front transitions in an eddy-resolving ocean GCM, *Geophys. Res. Lett.*, *37*, L23602, doi:10.1029/2010GL045386.

Trani, M., P. Falco, and E. Zambianchi (2011), Near-surface eddy dynamics in the Southern Ocean, *Polar Res.*, *30*, 11,203.

van Aken, H. M., H. Ridderinkhof, and W. P. M. de Ruijter (2004), North Atlantic Deep Water in the south-western Indian Ocean, *Deep Sea Res.*, *51*(6), 755–776.

van Wijk, E. M., S. R. Rintoul, B. M. Ronai, and G. D. Williams (2010), Regional circulation around Heard and McDonald Islands and through the Fawn Trough, central Kerguelen Plateau, *Deep Sea Res.*, *57*(5), 653–669.

Warren, B. A. (1981), Transindian hydrographic section at lat 18-degrees-S - Property distributions and circulation in the South Indian Ocean, *Deep Sea Res.*, *28*(8), 759–788.

Waterman, S., A. C. Naveira Garabato, and K. L. Polzin (2012), Internal waves and turbulence in the Antarctic Circumpolar Current, *J. Phys. Oceanogr.*, p. in press.

You, Y. Z. (2000), Implications of the deep circulation and ventilation of the Indian Ocean on the renewal mechanism of North Atlantic Deep Water, *J. Geophys. Res.*, *105*(C10), 23,895–23,926.